paranasal sinuses. *Int J Radiat Oncol Biol Phys* 2011;**81**:1473–8.
10. Lara PN, Redman MW, Kelly K *et al.* Disease control rate at 8 weeks predicts clinical benefit in advanced non-small-cell lung cancer: results from Southwest Oncology Group randomized trials. *J Clin Oncol* 2008;**26**:463–7.
11. Buyse M, Thirion P, Carlson RW *et al.* Relation between tumour response to first-line chemotherapy and survival in advanced colorectal cancer: a meta-analysis. Meta-Analysis Group in Cancer. *Lancet* 2000;**356**:373–8.
12. Kadish S, Goodman M, Wang CC. Olfactory neuroblastoma. A clinical analysis of 17 cases. *Cancer* 1976;**37**:1571–1576.
13. Eisenhauer EA, Therasse P, Bogaerts J *et al.* New response evaluation criteria in solid tumours: revised RECIST guideline (version 1.1). *Eur J Cancer* 2009;**45**:228–47.
14. Truong MT, Kamat UR, Liebsch NJ *et al.* Proton radiation therapy for primary sphenoid sinus malignancies: treatment outcome and prognostic factors. *Head Neck* 2009;**31**:1297–308.
15. Nishimura H, Ogino T, Kawashima M *et al.* Proton-beam therapy for olfactory neuroblastoma. *Int J Radiat Oncol Biol Phys* 2007;**68**:758–62.
16. Pommier P, Liebsch NJ, Deschler DG *et al.* Proton beam radiation therapy for skull base adenoid cystic carcinoma. *Arch Otolaryngol Head Neck Surg* 2007;**132**:1242–9.
17. Passero VA, Branstetter BF, Shuai Y *et al.* Response assessment by combined PET-CT scan versus CT scan alone using RECIST in patients with locally advanced head and neck cancer treated with chemoradiotherapy. *Ann Oncol* 2010;**356**:373–378.
18. Tahara M, Ohtsu A, Hironaka S *et al.* Clinical impact of criteria for complete response (CR) of primary site to treatment of esophageal cancer. *Jpn J Clin Oncol* 2005;**35**:316–23.
19. Zenda S, Hironaka S, Taku K *et al.* Optimal timing of endoscopic evaluation of the primary site of esophageal cancer after chemoradiotherapy or radiotherapy: a retrospective analysis. *Dig Endosc* 2009;**21**:245–51.
20. Hermans R, Pameijer FA, Mancuso AA *et al.* Laryngeal or hypopharyngeal squamous cell carcinoma: can follow-up CT after definitive radiation therapy by used to detect local failure earlier than clinical examination alone? *Radiology* 2000;**214**:683–7.
21. Forastiere AA, Goepfert H, Maor M *et al.* Concurrent Chemotherapy and Radiotherapy for Organ Preservation in Advanced Laryngeal Cancer. *NEJM* 2003;**349**:2091–8.
22. Lafebvre JL, Rolland F, Tesselaar M *et al.* Phase 3 randomized trial on larynx preservation comparing sequential vs alternating chemotherapy and radiotherapy. *J Natl Cancer Inst* 2009;**101**:142–152.
23. Ong SC, Schoder H, Lee NY *et al.* Clinical utility of 18F-FDG PET/CT in assessing the neck after concurrent chemoradiotherapy for Locoregional advanced head and neck cancer. *J Nucl Med* 2008;**49**:532–40.

Experimental evaluation of a spatial resampling technique to improve the accuracy of pencil-beam dose calculation in proton therapy

Yusuke Egashira[a)]
Department of Bioengineering, Graduate School of Engineering, University of Tokyo, 2-11-16, Yayoi, Bunkyo-ku, Tokyo 113-8656, Japan and Japan Society for the Promotion of Science, Ichibancho 8, Chiyoda-ku, Tokyo 102-8472, Japan

Teiji Nishio
Particle Therapy Division, Research Center for Innovative Oncology, National Cancer Center, Kashiwa, 6-5-1 Kashiwanoha, Kashiwa-shi, Chiba 277-8577, Japan

Taeko Matsuura
Department of Applied Molecular-Imaging Physics, Graduate School of Medicine, Hokkaido University, Sapporo, Hokkaido 060-8638, Japan

Satoru Kameoka
Particle Therapy Division, Research Center for Innovative Oncology, National Cancer Center, Kashiwa, 6-5-1 Kashiwanoha, Kashiwa-shi, Chiba 277-8577, Japan

Mitsuru Uesaka
Department of Bioengineering, Graduate School of Engineering, University of Tokyo, 2-11-16, Yayoi, Bunkyo-ku, Tokyo 113-8656, Japan

(Received 27 October 2011; revised 16 April 2012; accepted for publication 15 May 2012; published 11 June 2012)

Purpose: In proton therapy, pencil-beam algorithms (PBAs) are the most widely used dose calculation methods. However, the PB calculations that employ one-dimensional density scaling neglect the effects of lateral density heterogeneity on the dose distributions, whereas some particles included in such pencil beams could overextend beyond the interface of the density heterogeneity. We have simplified a pencil-beam redefinition algorithm (PBRA), which was proposed for electron therapy, by a spatial resampling technique toward an application for proton therapy. The purpose of this study is to evaluate the calculation results of the spatial resampling technique in terms of lateral density heterogeneity by comparison with the dose distributions that were measured in heterogeneous slab phantoms.

Methods: The pencil beams are characterized for multiple residual-range (i.e., proton energy) bins. To simplify the PBRA, the given pencil beams are resampled on one or two transport planes, in which smaller sub-beams that are parallel to each other are generated. We addressed the problem of lateral density heterogeneity comparing the calculation results to the dose distributions measured at different depths in heterogeneous slab phantoms using a two-dimensional detector. Two heterogeneity slab phantoms, namely, phantoms A and B, were designed for the measurements and calculations. In phantom A, the heterogeneity slab was placed close to the surface. On the other hand, in phantom B, it was placed close to the Bragg peak in the mono-energetic proton beam.

Results: In measurements, lateral dose profiles showed a dose reduction and increment in the vicinity of $x = 0$ mm in both phantoms at depths $z = 142$ and 161 mm due to lateral particle disequilibrium. In phantom B, these dose reduction/increment effects were higher/lower, respectively, than those in phantom A. This is because a longer distance from the surface to the heterogeneous slab increases the strength of proton scattering. Sub-beams, which were generated from the resampling plane, formed a detouring/overextending path that was different from that of elemental pencil beams. Therefore, when the spatial resampling was implemented at the surface and immediately upstream of the lateral heterogeneity, the calculation could predict these dose reduction/increment effects. Without the resampling procedure, these dose reduction/increment effects could not be predicted in both phantoms owing to the blurring of the pencil beam. We found that the PBA with the spatial resampling technique predicted the dose reduction/increment at the dose profiles in both phantoms when the sampling plane was defined immediately upstream of the heterogeneous slab.

Conclusions: We have demonstrated the implementation of a spatial resampling technique for pencil-beam calculation to address the problem of lateral density heterogeneity. While further validation is required for clinical use, this study suggests that the spatial resampling technique can make a significant contribution to proton therapy. © *2012 American Association of Physicists in Medicine.* [http://dx.doi.org/10.1118/1.4722984]

Key words: proton therapy, treatment planning, dose calculation, pencil-beam algorithm

I. INTRODUCTION

Passive scattering proton therapy has been widely implemented in many proton therapy facilities around the world. In proton therapy, it is most important to concentrate and conform the proton dose distributions to the tumor by utilizing the Bragg peak. Pencil-beam algorithms (PBA; Refs. 1–11) have been the most commonly used dose calculation method for charged-particle radiation therapy. In the PBA by Hong *et al.*,[3] the accuracy of the PBA is guaranteed in homogeneous material with reasonable computing time. However, the PBA calculations that employ one-dimensional density scaling neglect the effects of lateral density heterogeneity on the dose distributions, whereas some particles included in such pencil beams could overextend beyond the interface of the density heterogeneity.

Several techniques for addressing the problem of lateral density heterogeneities have been introduced into the PBAs. In the PB calculations that employ one-dimensional density scaling, elemental pencil beams were split into subbeams, which are smaller than an elemental pencil beam.[5–8] Schaffner *et al.*[5,6] reduced the over-reaching of protons by splitting each scanning beam into small virtual pencil beams for dose calculation on the patient surface. In the pencil-beam splitting algorithm,[7,8] each pencil beam is dynamically split into smaller ones, up to 4 × 4 Gaussian near the lateral density interface. For efficient dose calculation, split pencil beams are densely set as necessary; otherwise, large pencil beams are sparsely set. Two-dimensional density scaling,[9] namely, scaling of the lateral proton fluence, of the PB calculation has also improved the calculation accuracy around lateral density heterogeneities. However, the problem of lateral density heterogeneity is not new, and has been approached to improve the dosimetric accuracy of the pencil-beam calculation for electron therapy.[11,12] For example, the Fermi-Eyges theory[10] has been applied to the PB calculation for electron therapy. The pencil-beam redefinition algorithm (PBRA; Refs. 11 and 12) handles the electron flow and energy at the calculation plane in accordance with this theory. For the dose calculation and beam transportation, three physical quantities were required. Fluence, mean direction, and rms spread about the mean direction are characterized for multiple energy bins for a given pencil beam. The width of energy bins, which is typically defined as 0.5–1.0 MeV, determines the spectrum of the electron energy. When 5.0 mm interval between the redefinitions was used, it required 10–20 times pencil-beam redefinition for a 9–20 MeV electron beam. Since the rms spread about the mean direction of electrons immediately after the redefinition is minimal, the PB redefinition calculation improved the accuracy of pencil-beam dose calculation for electrons in the presence of heterogeneity. A similar idea to the PBRA was applied to heavy particles for beam customization, in which particle flow in the transverse plane was considered in the absence of heterogeneity.[13] In the presence of lateral heterogeneities, however, the concept of the PBRA has not been evaluated for dose calculation in proton therapy.

In this paper, a spatial resampling technique for pencil-beam calculation (SRPBA) is described. The concept of the spatial resampling technique is simplification of the PBRA toward the application of proton therapy. Provided that the PBRA is implemented for clinical proton therapy with no modification, the resultant number of energy bins will considerably increase owing to the compensator and the range modulator. While electrons can be scattered through very large angles so that their path is considerably modified, protons scatter by a few degrees and follow an only slightly nonstraight path. With the spatial resampling technique, the pencil beams that are defined with multiple residual-range (i.e., proton energy) bins are resampled on one or two transport planes. In addition, the mean directions of resampled subbeams are defined as parallel to each other. As a consequence of the spatial resampling technique, the SRPBA can similarly address the problem of lateral density heterogeneity. The purpose of this study is to evaluate the spatial resampling technique in terms of lateral density heterogeneity by the measurements in heterogeneous slab phantoms.

II. MATERIALS AND METHODS

II.A. Pencil-beam algorithm

In the PBA by Hong *et al.*,[3] the full beam is represented by a set of elemental pencil beams as follows:

$$D_{\mathrm{PBA}}(x,y,z) = \iint dx'dy' \cdot \Phi_0(x',y') \times \frac{C(x',y',\mathrm{WEL}(x',y',z))}{2\pi\left[\sigma_{\mathrm{PBA}}(x',y';z)\right]^2} \times \exp\left(-\frac{(x'-x)^2+(y'-y)^2}{2\cdot\left[\sigma_{\mathrm{PBA}}(x',y';z)\right]^2}\right), \quad (1)$$

$$\sigma^2_{\mathrm{PBA}}(x',y';z) = \sigma^2_{\mathrm{line,PBA}} + \sigma^2_{\mathrm{comp,PBA}} + \sigma^2_{\mathrm{pt,PBA}}, \quad (2)$$

$$\sigma^2_{\mathrm{line,PBA}} = \sigma^2_{\mathrm{size}} \cdot \left(\frac{\mathrm{airgap}+z}{d_{\mathrm{bld}}}\right)^2, \quad (3)$$

$$\sigma^2_{\mathrm{comp,PBA}} = \left(\frac{t}{2}+\mathrm{airgap}+z\right)^2 \cdot \sigma^2_{\theta}, \quad (4)$$

where $\Phi_0(x, y)$ is the fluence of the open beam and the integration is over the beam area. $C(x', y', \mathrm{WEL}(x', y', z))$ is the central-axis term of the dose distributions of the pencil beam located at (x', y'), including an inverse square correction. $\mathrm{WEL}(x', y', z)$ corresponds to water-equivalent length from the source to the point of interest (x', y', z). σ_θ is the characteristic scattering angle of range compensator calculated with the Highland formula.[14,15] The origin of the z axis is set to the surface of a patient. The total Gaussian beam size (standard deviation), so-called Gaussian-sigma, is composed of three components: (i) the effective source size σ_{size}, (ii) spatial spread due to scattering of the range compensator σ_{comp}, and (iii) spatial spread due to multiple scattering within the patient σ_{pt}. $\sigma_{\mathrm{PBA}}(x, y; z)$ is obtained by adding in quadrature the contributions from (i) to (iii). d_{bld} is the distance from the source to the downstream face of the aperture collimator.

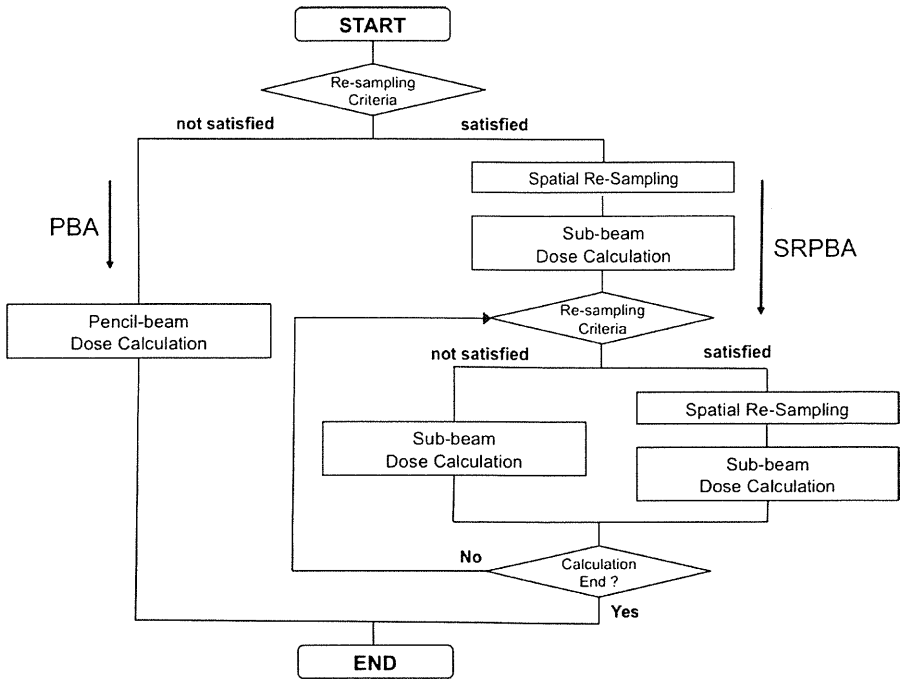

FIG. 1. Flow diagram of a spatial resampling technique for pencil-beam calculation (denoted as SRPBA). The resampling criteria (a) and (b) determine if pencil beams are resampled or not.

Airgap indicates the distance from the downstream face of the aperture collimator to the patient surface. t is the thickness of the range compensator.

II.B. Implementation of spatial resampling technique

The spatial resampling technique for pencil-beam calculation is the application of the PBRA proposed for electron beam therapy.[11,12] The PBRA requires three physical parameters, namely, fluence, mean direction, and spatial spread about the mean direction. The fluence is assumed to be uniform at the entrance to a range compensator and zero outside the aperture downstream of the range compensator. The mean direction of the protons for each elemental pencil beam emanated from the virtual source defines the direction of fan lines. The spatial spread about the mean direction for elemental pencil beams is obtained from Eq. (2). It is noteworthy that these physical quantities are characterized for multiple residual-range (i.e., proton energy) bins for given pencil beams.

Figure 1 shows a flow diagram of the spatial resampling procedure. For the calculation of protons, the number of redefinition planes could be reduced owing to a small scatter effect compared with that of electrons. Pencil beams generated at the entrance to the compensator are propagated to the patient surface including the effect of the scattering from the compensator and airgap from the downstream face of the aperture to the patient surface. The range modulator is treated as a set of degraders with weight factor.[16] The resampling procedure is implemented first at the patient surface with three physical parameters only when the spatial spread of the beams exceeds the calculation grid size. In other words, the first resampling criterion can be given as follows:

$$\sigma_{\mathrm{PBA}}(x', y'; z = 0) > \delta_{xy}, \tag{5}$$

where δ_{xy} is the grid size. Otherwise, if the first resampling criterion is not satisfied, the dose calculation by the other pencil beams follows the conventional one. For each range bin, at the resampling plane, the spatial spread of sub-beams is given by Eq. (A1) of Appendix A for each range bin. In addition, for simplification, the mean direction for all pencil beams is the same, and they are parallel to the beam axis. The sub-beam can be additionally resampled at an arbitrary plane, in which these beams satisfy the second criterion in terms of the fluence and the spatial spread to avoid unnecessary resampling. The secondary resampling criteria are given as follows:

$$\frac{[\Phi(x, y; z = 0)]_{R_{\mathrm{res}}(x,y;z=d_{\mathrm{smp}})}}{\sum_{R'=0}^{R_0}[\Phi(x, y; z = 0)]_{R'}} > \kappa_\Psi \quad \text{and}$$

$$\sigma_{\mathrm{SR_n}}(x, y; z = d_{\mathrm{smp}}) > \delta_{xy}, \tag{6}$$

where $[\Phi(x, y, ; z = 0)]_R$ is the fluence of the pencil beam per residual range R at the surface $(x, y, 0)$. $\sigma_{\mathrm{SR_n}}(x, y; d_{\mathrm{smp}})$ corresponds to the sigma of sub-beams at a depth of $z = d_{\mathrm{smp}}$ which is the secondary resampling depth. The parameters for these criteria $\sigma_{\mathrm{SR_n}}$ and $[\Phi(x, y, ; z = 0)]_R$ are given by Eqs. (A1) and (A6), respectively. R_0 is the initial residual range of pencil beam. To avoid the spatial resampling of the beams with a relatively small number of particles, the cutoff parameter κ_Ψ was chosen as 0.1. The number of resamplings is restricted to two: one at the surface plane and another inside the patient. All beams are propagated using one-dimensional density scaling until all protons are stopped. The relative dose

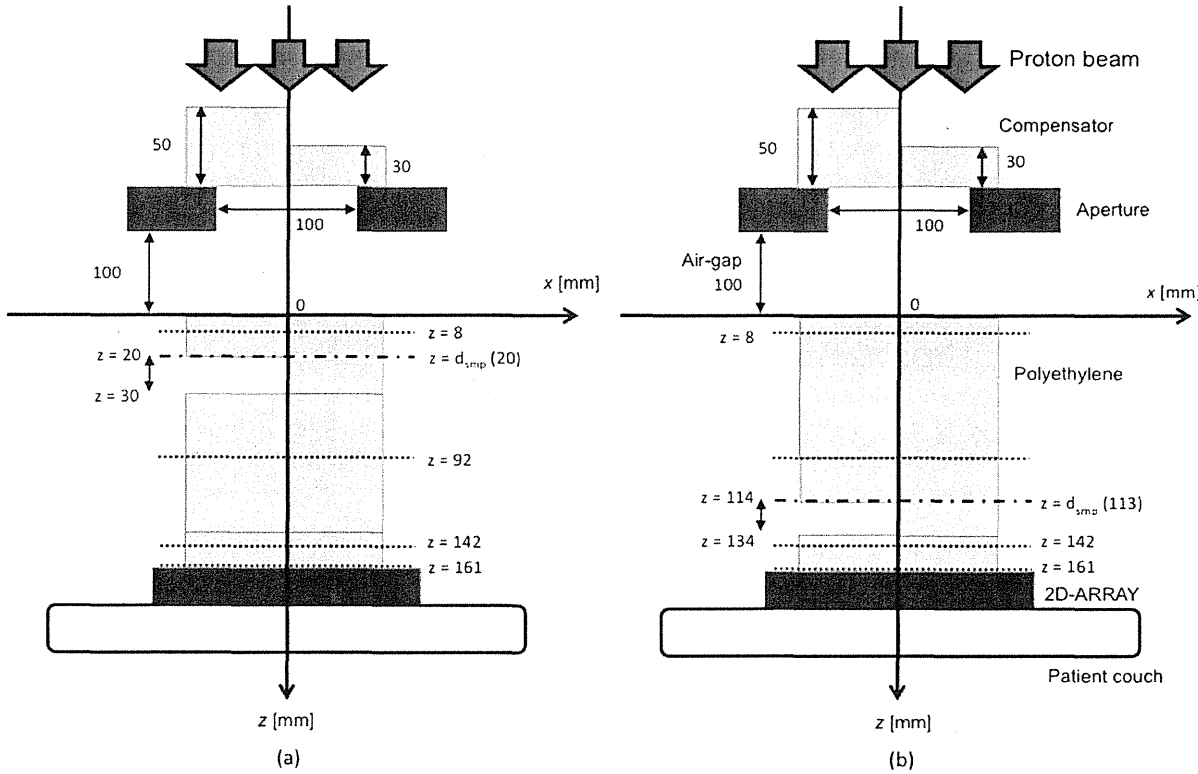

FIG. 2. Experimental arrangements for measurement. Polyethylene blocks were stacked as (a) phantom A and (b) phantom B. The dotted and dashed lines show the measurement and sampling planes, respectively.

for deposition in a patient voxel could be obtained from the measured depth-dose distributions in water. Details of the calculation of fluence and dose distributions are described in Appendix B. The spatial resampling technique for pencil-beam algorithm was implemented with 1 mm resolution using a 2.8 GHz Intel Core 2 Duo processor on an Apple iMac computer. In addition, the calculation result with this technique was compared to the conventional PBA described in Sec. II.A.

II.C. Beam line system and experimental geometry

At the National Cancer Center East (NCCE), Japan, 235 MeV protons accelerated by AVF cyclotron can be transported into three ports. For clinical use, two of the three ports have a rotating gantry, and the other has a horizontal fixed port.[17,18] In this study, 190 MeV proton beams were sent to the rotating gantry, and laterally uniform dose distributions were obtained by the dual-ring double-scattered method.[19]

We examined the PBA with or without the spatial resampling technique by comparing the calculation results with the experimentally measured dose distributions in heterogeneous slab phantoms. A PTW 2D Array seven29™ (PTW, Freiburg, Germany) was used as a proton dose detector.[20,21] This is a two-dimensional detector matrix with 729 uniformly arranged ionization chambers in a 10 mm pitch 27 × 27 array. The sensitive volume of a unit chamber is 5 mm × 5 mm × 5 mm. The ionization chambers of the array are open to the air. The offset thickness from the entrance surface to the center of the sensitive volume is 8 mm in water-equivalent thickness.[21] In order to compare the calculation results and measurements under the same conditions, we corrected the depth calculation by the offset thickness when calculating the dose distributions. We also convolved the calculation results with the detector cell size of 5 mm × 5 mm. The heterogeneous slab phantoms in Fig. 2 were used for verification of the spatial resampling technique. We investigated proton detouring and overextension effects, that is, lateral density heterogeneity effects, on dose distributions using a mono-energetic 190 MeV proton beam. As shown in the figure, two phantoms (A and B) were designed by stacking L-shaped polyethylene and polyethylene plates. The water-equivalent thickness of polyethylene was 1.02. In phantom A, the depth of the low-density region (air) was located at depths from $z = 30$ mm to 50 mm, which is the plateau of the depth-dose curve. On the other hand, in phantom B, the interface between air and polyethylene was located at depths from $z = 114$ mm to 134 mm, which is close to proton range. Lateral dose distributions were measured at depths of $z = 8$ mm, 92 mm, 142 mm, and 161 mm with changing thickness of the polyethylene plate. The air-gap between the rectangular aperture of 100 mm × 100 mm and the surface of the phantom was fixed at 100 mm. Since the chamber pitch was 10 mm, we shifted the detector by 5 mm in the x direction to merge measurements with a lateral sampling pitch of 5 mm. In the calculation, parallel pencil beams were generated at the entrance to the range

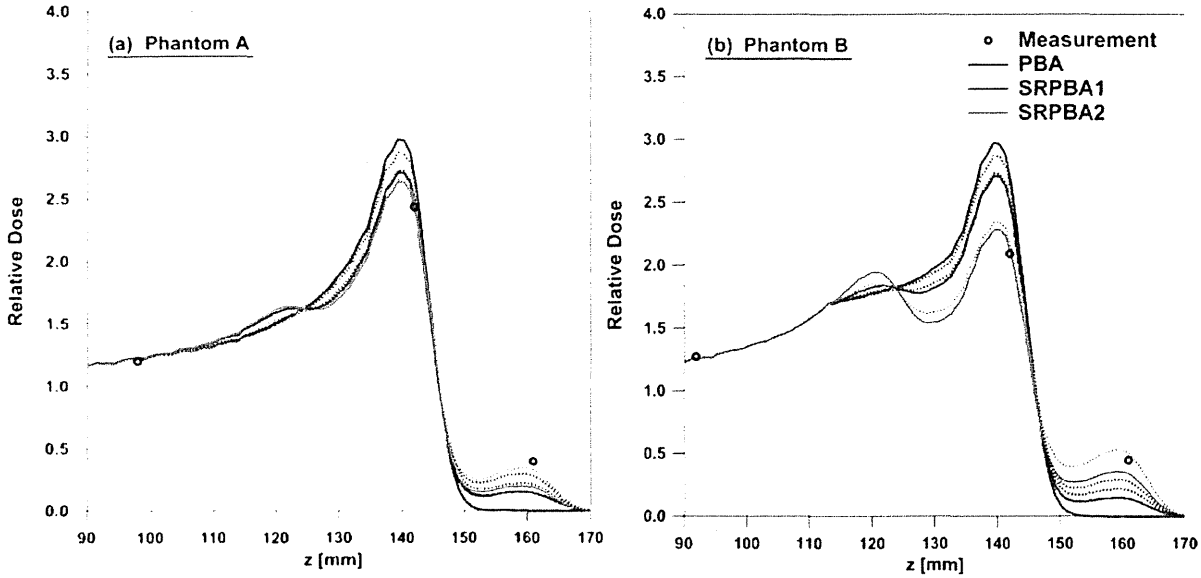

FIG. 3. Depth-dose profiles in (a) phantom A and (b) phantom B: Red, blue, and green solid lines depict calculation results using the PBA, the one with the resampling only at $z = 0$ (denoted as SRPBA1) and the one with the resampling at $z = 0$ and $z = d_{smp}$ (denoted as SRPBA2), respectively. Dashed lines depict calculation results considering 1 mm misalignment. In addition, open circle indicates measurements.

compensator because we are interested in the middle of the field, in which density interface was placed. With the spatial resampling technique implemented at $z = 0$ and $z = d_{smp}$, the depths of $d_{smp} = 30$ mm and 113 mm were chosen as those for secondary resampling in phantoms A and B, respectively. These depths correspond to those of the density interface between polyethylene and air in the phantoms. In order to consider the setup error of the phantom, all calculations were also carried out with 1 mm misaligned geometry from $x = 0$. All the dose data sets were normalized at a point ($x = -30$ mm, $y = 0$ mm, $z = 8$ mm) in a flat dose region for comparison of measurements and calculations.

III. RESULTS AND DISCUSSION

We addressed the problem of the lateral density heterogeneity comparing the calculation results to the dose distributions measured at different depths in heterogeneous slab phantoms using a two-dimensional detector. Figures 3 and 4 show comparisons of the depth and lateral dose profile obtained from measurements, the PB calculation with or without the spatial resampling technique. As shown in Fig. 3, the main and potential Bragg peaks appeared in the vicinity of the depths of $z = 140$ mm and $z = 160$ mm, respectively. Lateral dose profiles are shown in Figs. 4(a) and 4(b) at a depth of $z = 142$ mm of phantoms A and B, respectively. In measurements, both lateral dose profiles showed dose reduction in the vicinity of $x = 0$ mm owing to lateral particle disequilibrium.[23] As shown in Figs. 4(c) and 4(d), at a depth of $z = 161$ mm, both lateral dose profiles showed dose increment in the vicinity of $x = 0$ mm. When the spatial resampling was implemented, in phantom A, the minimal sub-beam could predict these dose reduction/increment effects. Without the resampling, the calculation could not reproduce these results because of the elemental pencil beams, which were substantially blurred by multiple Coulomb scattering. In phantom B, the calculation could predict these dose reduction/increment effects only when the spatial resampling was implemented at the surface and immediately upstream of the lateral heterogeneity. For quantitative evaluation of the accuracy in the density interface in the middle of the field, the difference of relative dose between $x = -25$ and 25 mm, which corresponds to half of the irradiation field, was calculated as follows:

$$\text{(Difference of relative dose)} = D_c(x) - D_m(x), \quad (-25 \le x \le 25 \text{ mm}), \tag{7}$$

where $D_c(x)$ and $D_m(x)$ are the calculated dose and the measured dose, respectively. Figure 5 shows a summary of the difference of relative dose. In summary, more resampling procedures improved the accuracy. In phantom A, the difference of relative dose of the PBA (without resampling), the PBA with resampling only at $z = 0$ and the PBA with resampling at $z = 0$ mm and $z = d_{smp}$ were within ± 0.48, ± 0.35, and ± 0.31, respectively. On the other hand, in phantom B, the relative dose difference of the PBA, the SRPBA (resampled at $z = 0$), and the SRPBA (resampled at $z = 0$ mm and $z = d_{smp}$) were within ± 0.65, ± 0.53, and ± 0.28, respectively. Without the spatial resampling, in phantom A, the calculation could not reproduce this dose reduction with $+10.7\%$ at $x = 0$ while the SRPBA could reproduce it within 1.5% when the setup error of 1 mm was taken into account. In phantom B, on the other hand, only the PBA with resampling at $z = 0$ and $z = d_{smp}$ could reproduce this dose reduction with 0.4% at $x = 0$ because the smaller size of resampled beam correctly predicted the lateral dose perturbation.

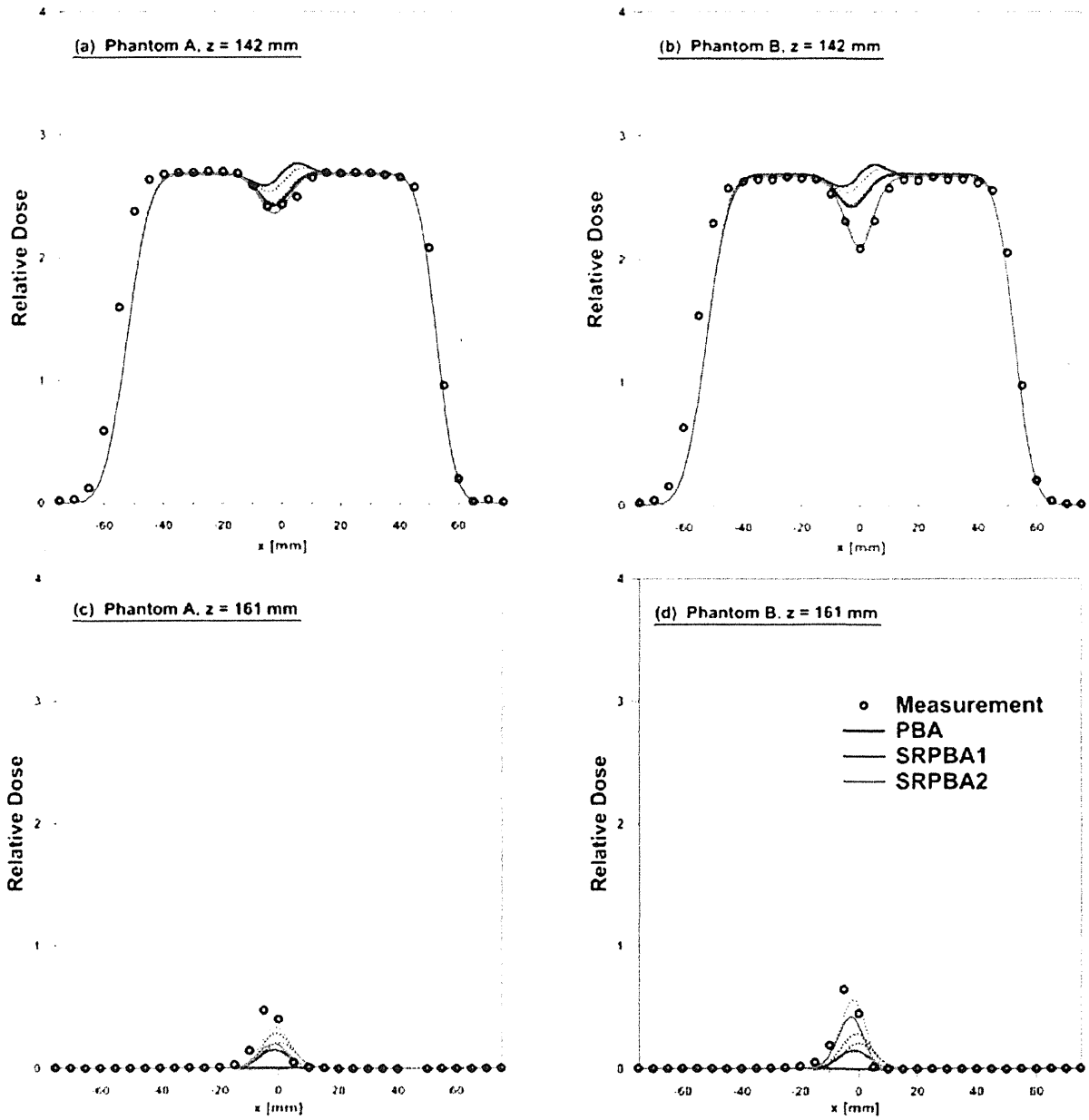

FIG. 4. Lateral dose profiles in the phantoms: Solid lines depict calculation results using the PBA, the one with the resampling only at $z = 0$ (denoted as SRPBA1) and the one with the resampling at $z = 0$ and $z = d_{\text{smp}}$ (denoted as SRPBA2). Dashed lines depict calculation results considering 1 mm misalignment. In addition, open circle indicates measurements.

While the experimental geometries that we used might be somewhat simple, they were effective for investigation of the lateral density heterogeneity effect of protons.[7,21,22] This is because the effect by the detouring/overextension of protons appeared as characteristic regions in the dose profiles. The geometry is illustrated in Fig. 6 for the case of phantom B of a parallel beam of protons impinging on two air/polyethylene interfaces in the range compensator and the heterogeneity slab phantom. The strength of multiple Coulomb scattering depends on the compensator thickness as given in Eq. (4). Therefore, the dose is primarily perturbed just below the range compensator (i.e., scattering-in and scattering-out of protons) owing to the difference of its thickness on sides 1 and 2. That is, as pointed out by Goitein,[23] protons on side 1 are more scattered by the compensator than on side 2. In the phantom, protons are transported to the density interface at $z = 114$ mm inside the phantom as they are scattered by polyethylene. A region such as A in Fig. 6 is traversed both by protons on side 1 and by some protons that came from side 2. Note that protons on side 1 and some protons that came from side 2 have

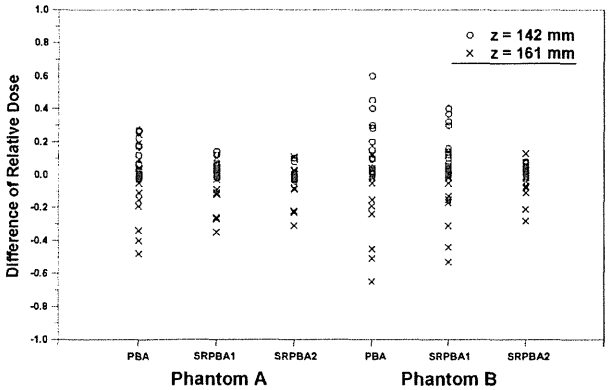

FIG. 5. Difference of relative dose between $x = -25$ and 25 mm: Calculation results which include the PBA, the one with the resampling only at $z = 0$ (denoted as SRPBA1) and the one with the resampling $z = 0$ and $z = d_{\mathrm{smp}}$ (denoted as SRPBA2) minus measurements. Red open circle and blue cross depict the relative dose difference at depths $z = 142$ mm and $z = 161$ mm, respectively. The misalignment and nonmisalignment cases are merged in this figure.

different residual range (i.e., energy) due to the difference of the compensator thickness. In region B, the opposite occurs. Subsequently, protons from side 1 traverse the inhomogeneity (air), in which they are much less scattered than on side 2. Away from the density interface, the Bragg peak is formed around depth $z = 140$ mm. However, some protons from regions A and B, namely, detouring and overshooting protons, form Bragg peaks in the vicinity of $z = 120$ mm and 160 mm, respectively. Kanematsu *et al.*[7] and Hotta *et al.*[21] have reported the effect of detouring protons using similar geometry. Furthermore, we experimentally elucidated such effect on the proton dose distributions in the case that the depth of the inhomogeneous slab (air) was changed. The longer distance from the surface to the heterogeneous slab increased the strength of proton scattering. The number of protons from side 1 (or 2) at region B (or A) increased more in phantom B than in phantom A. In phantom B where the slab was placed in a deep region, therefore, this dose reduction was higher than that in phantom A where the slab was placed in a shallow region. For the same reason, the magnitude and the shape of the potential peak which were formed by the overshooting protons in phantom A were relatively small and spread compared with those in phantom B. Figure 7 shows the lateral dose profile at a depth of $z = 142$ mm, which corresponds to the main Bragg peak of phantom B. In the figure, the solid lines indicate the calculation results with changing of the secondary resampling depth from 14 mm to 113 mm. For comparison, the dose profile without spatial resampling is shown as well. Without the resampling procedure, the scattering-in and scattering-out effects of protons between sides 1 and 2 could not be predicted in the vicinity of the density heterogeneity owing to the blurring of pencil beams. In the calculation with the spatial resampling, sub-beams formed a detouring/overextension path that was different from elemental pencil beams, and predicted the lateral particle disequilibrium in the shadow of the

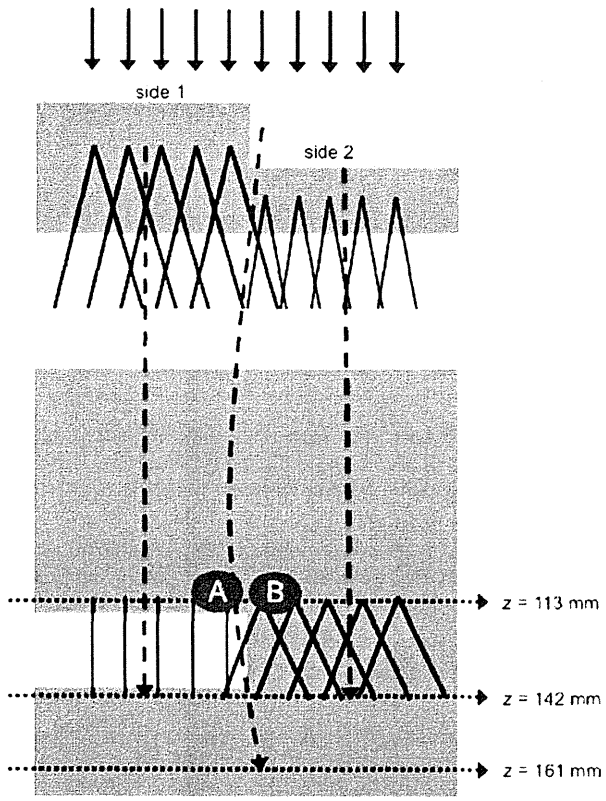

FIG. 6. Schematic drawing of an L-shaped compensator and phantom B intersecting a broad beam. Away from the interface between the two media (air /polyethylene), protons form the Bragg peak around depth $z = 142$ mm (dashed straight lines). On the other hand, close to the interface region such as A, protons are overextended (dashed curved line).

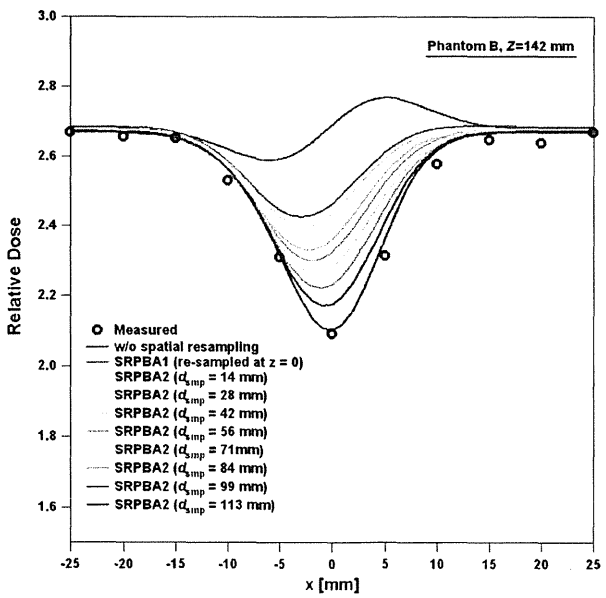

FIG. 7. Lateral dose profiles at $z = 142$ mm in phantom B upon changing the resampling depth of $z = d_{\mathrm{smp}}$. Solid lines depict calculation results and open circles depict measurement data.

inhomogeneity. Thus, dose reduction and increment appeared in the lateral dose profiles of the calculation result by the spatial resampling. The accuracy of dose reduction adjacent to $x = 0$ mm was improved as the additional resampling depth was close to the heterogeneity interface. This is because proton disequilibrium shown in the dose profile was caused by the scattering from the compensator and the polyethylene from $z = 0$ mm to $z = 114$ mm. Therefore, the spatial resampling should be implemented immediately upstream of the lateral heterogeneity.

Indeed, in clinical situations, protons pass through more complicated structures such as soft tissue, bone, and air before they stop. These particles show detouring and overextension effects due to multiple Coulomb scattering, and their trajectories are not straight. Moreover, organs at risk often surround a target, especially in the head and neck region. In proton therapy with passive scattering method, the range spectra at the surface can be complicated due to the proton scattering from the range compensator. In this study, the number of range bins was up to two because of the L-shaped compensator and the simple lateral heterogeneity. The shape of the target and human heterogeneity determine the shape of the range compensator. Therefore, the complicated shape of the compensator and human heterogeneities increase the number of residual-range bins on the sampling plane.[24] In treatment planning, there are always trade-offs between accuracy and time. In the calculation of the spatial resampling for the H&N tumor, as described in Appendix C, the increases in computing time were by factors of 9 and 20 for one and two spatial resamplings, respectively, compared with the pencil-beam calculation without this technique. Although more resampling would improve the calculation accuracy for realistic radiotherapy applications, resampling more than three planes might be an extensive numerical task and less practical in the treatment planning process due to its time-consuming nature. The accuracy of the spatial resampling technique strongly depends on the secondary resampling depth while the setting at the appropriate depth improves the accuracy. An optimal way to choose d_{smp} may be determined by measurements in an anthropomorphic phantom or by Monte Carlo calculations for more realistic geometries. The number of residual-range bins also depends on the quantization level of the residual-range spectra. As future work, therefore, these parameters should be carefully set throughout the verification of many other realistic cases as future work. Also, a quantitative comparison between the SRPBA and the Schaffner *et al.* algorithm will be needed for a next step.

IV. CONCLUSIONS

We have demonstrated the implementation of the spatial resampling technique for pencil-beam calculation to approach the problem of lateral density heterogeneity in proton therapy. The PBRA that was proposed by Shiu and Hogstrom was simplified as the spatial resampling technique for proton therapy. In the calculation, the fluence was characterized for multiple residual-range (i.e., proton energy) bins for given pencil beams, and spatially resampled on one or two transport planes. We addressed the problem of lateral density heterogeneity comparing the calculation results to the dose distributions measured at different depths in heterogeneous slab phantoms using a two-dimensional detector. In the measurements of slab phantoms, we found that the spatial resampling technique for pencil-beam calculation reproduced the characteristic dose reduction/increment at the dose profiles when the sampling plane was defined immediately upstream of the heterogeneous slab. The spatial resampling technique could improve the accuracy of pencil-beam calculation using one-dimensional density scaling. While further validation is required for clinical use, this study suggests that the spatial resampling technique as the application of PBRA can make a significant contribution to proton therapy.

ACKNOWLEDGMENTS

The authors are grateful to Dr. Ryosuke Kohno and Dr. Kenji Hotta for useful discussions. They also wish to thank SHI Accelerator Service, Ltd., for their help with measurements at the proton therapy facilities at the National Cancer Center, Kashiwa. Y.E. received a grant from the Japan Society for the Promotion of Science for Young Scientists. This work was partly supported by Health and Labour Science Research Grants from the Japanese Government.

APPENDIX A: SPATIAL SPREAD OF SUB-BEAM

In this Appendix, we summarize the spatial spread of the sub-beam (i.e., pencil beam generated from the resampled planes). Like $\sigma_{\mathrm{PBA}}(z)$ shown in Eq. (2), the approximated Gaussian-sigma of sub-beam $\sigma_{\mathrm{SR_n}}(z)$ at arbitrary depth z is composed of three components,

$$\sigma^2_{\mathrm{SR_n}}(z) = \sigma^2_{\mathrm{line,SR_n}}(z) + \sigma^2_{\mathrm{comp,SR_n}}(z) + \sigma^2_{\mathrm{pl,SR_n}}(z). \quad \text{(A1)}$$

In the spatial resampling technique, we extended these terms as follows. From Eq. (3), we defined the following Gaussian-sigma $\sigma_{\mathrm{line,SR_n}}(z)$ with respect to the effective source size σ_{size} as follows:

$$\sigma^2_{\mathrm{line,SR_n}}(z) = \begin{cases} \{h(\mathrm{airgap})/z\} \cdot \sigma^2_{\mathrm{line,PBA}}(\mathrm{airgap} = 0) & (0 < z \le d_{\mathrm{smp}}), \\ \{(h(\mathrm{airgap}) + \eta \cdot g(\sigma_{\mathrm{size}}))/z\} \cdot \sigma^2_{\mathrm{line,PBA}}(\mathrm{airgap} = -d_{\mathrm{smp}}) & (z > d_{\mathrm{smp}}), \end{cases}$$
$$h(\mathrm{airgap}) = \alpha_1 \cdot \mathrm{airgap} + \beta_1,$$
$$g(\sigma_{\mathrm{size}}) = \alpha_2 \cdot \sigma^2_{\mathrm{size}} + \beta_2 \cdot \sigma_{\mathrm{size}} + \gamma_2, \quad \text{(A2)}$$

where R_0 is the residual range of the open beam. η is d_{smp}/R_0. The correction factors $h(\mathrm{airgap})$ and $g(\sigma_{\mathrm{size}})$ are required in order to minimize the difference between σ_{PBA} and σ_{SR} in air. On the basis of the nominal energies of protons of 150 MeV, 190 MeV,

and 235 MeV that are used in the NCCE, Japan, the fitting parameters α_1, β_1, α_2, β_2, and γ_2 were calculated and are shown in Table I. Second, by the expansion of Eq. (4), $\sigma^2_{\text{comp,PBA}}(z)$ is extended

$$\sigma^2_{\text{comp,PBA}}(z) = \begin{cases} \sigma^2_{\text{comp,PBA}}(0) + \left\{2z \cdot \left(\frac{t}{2} + \text{airgap}\right) + z^2\right\} \cdot \sigma^2_\theta & (0 < z \le d_{\text{smp}}) \\ \sigma^2_{\text{comp,PBA}}(d_{\text{smp}}) + \left\{2(z - d_{\text{smp}}) \cdot \left(\frac{t}{2} + \text{airgap} + d_{\text{smp}}\right) + (z - d_{\text{smp}})^2\right\} \cdot \sigma^2_\theta & (z > d_{\text{smp}}) \end{cases}$$

$$= \sigma_0^2 + \sigma^2_{\text{comp,SR}_n}(z), \tag{A3}$$

where the first term σ_0^2 represents the spatial spread at the sampling depth $z = 0$ or d_{smp}, which corresponds to $\sigma_{\text{comp, PBA}}(0)$ or $\sigma_{\text{comp, PBA}}(d_{\text{smp}})$, respectively. Only the second term $\sigma^2_{\text{comp,SR}_n}(z)$ depends on the depth that is deeper than the sampling depth. Therefore, the spatial spread due to scattering of the range compensator in this technique is given as follows:

$$\sigma^2_{\text{comp,SR}_n}(z) = \begin{cases} \left\{2z \cdot \left(\frac{t}{2} + \text{airgap}\right) + z^2\right\} \cdot \sigma^2_\theta & (0 < z \le d_{\text{smp}}) \\ \left\{2\left(z - d_{\text{smp}}\right) \cdot \left(\frac{t}{2} + \text{airgap} + d_{\text{smp}}\right) + \left(z - d_{\text{smp}}\right)^2\right\} \cdot \sigma^2_\theta & (z > d_{\text{smp}}). \end{cases} \tag{A4}$$

Finally, the third component of $\sigma_{\text{pt, SR}}$ with respect to the multiple scattering within the patient[4] is calculated as follows:

$$\sigma^2_{pt,\text{SR}_n}(z) = \begin{cases} \sigma^2_{\text{pt,PBA}}(z, R_{\text{res}}(0)) & (0 < z \le d_{\text{smp}}), \\ \sigma^2_{\text{pt,PBA}}(z - d_{\text{smp}}, R_{\text{res}}(d_{\text{smp}})) & (z > d_{\text{smp}}), \end{cases} \tag{A5}$$

where $\sigma_{pt,\,PBA}$, which is modeled as a function of the distance and the residual range in the one-dimensional scaling approximation, is the multiple scattering within the patient.[3] $R_{\text{res}}(0)$ and $R_{\text{res}}(d_{\text{smp}})$ are the residual ranges at depth = 0 and d_{smp}, respectively. $\sigma_{\text{pt,SR}_n}$ is also infinitesimally small at the depth $z = \text{d}z$ or $d_{\text{smp}} + \text{d}z$. For example, the beam size σ_{PBA} and σ_{SR_n} in depth in water are displayed in Fig. 8. The calculations were performed for energy typical in proton radiation therapy, that is, 190 MeV. The effective source size was set to 22.7 mm in agreement with the nozzle at NCCE. It was located at above 2745 mm from the isocenter, namely, 2645 mm from $z = 0$ plane. A 30-mm-thick flat range compensator was inserted in the beam line, which corresponds to σ_θ of 17.4 mmrad. The airgap between the compensator and the patient surface was chosen as 100 mm. σ_{PBA} is equal to 2.3 mm at a depth of $z = 0$.

APPENDIX B: CALCULATION OF FLUENCE AND DOSE DISTRIBUTIONS

In this Appendix, we summarize the calculation of the fluence and dose distributions. At the surface $(x,y,0)$, the fluence of the pencil beam per residual range $[\Phi(x, y; z = 0)]_R$ is represented as follows:

TABLE I. Fitting parameters for determination of the correction factors h(airgap) and $g(\sigma_{\text{size}})$.

	h(airgap)		$g(\sigma_{\text{size}})$		
Nominal energy (MeV)	α_1	β_1	α_2	β_2	γ_2
150	1.9894	70.062	0.840	−129.18	4115.1
190	2.1370	68.486	3.2176	−301.79	7393.7
235	2.2654	76.587	9.4454	−699.28	14676

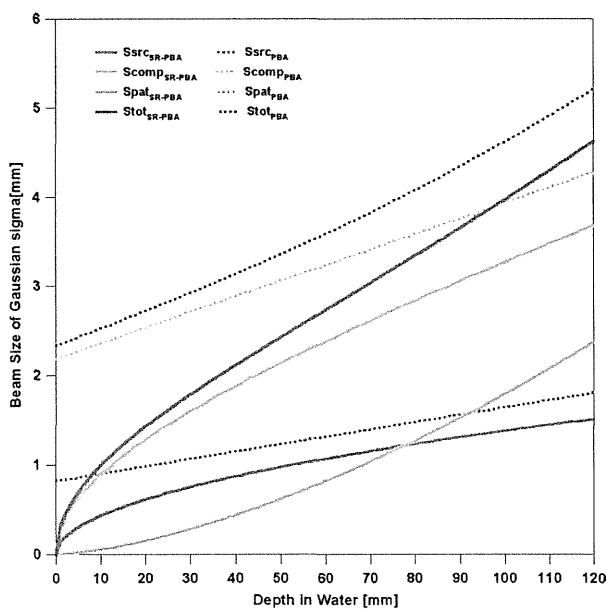

FIG. 8. Example of relationship between depth in water and beam size of Gaussian-sigma at the surface, when the 190 MeV mono-energetic proton beam is used. Thickness of range compensator is 30 mm and air-gap between the aperture and surface is 100 mm. Dotted and solid lines represent the beam size in the PBA and in the PBA with the spatial resampling, respectively. S_{src}, S_{comp} and S_{pat} lines show the beam size components due to the effective source size, scattering of the range compensator and multiple scattering within the patient, respectively. $S_{\text{pat-SRPBA}}$ overlaps $S_{\text{pat-PBA}}$. S_{tot} represent the overall Gaussian-sigma.

$$[\Phi(x, y; z = 0)]_g = \sum_{y'}\sum_{x'} \Delta x'\Delta y' \frac{\Phi_0(x', y')}{S} \times \exp\left(-\frac{(x-x')^2+(y-y')^2}{2\left[\sigma_{\mathrm{PBA}}(x', y'; z=0)\right]^2}\right) \times H(v_{\mathrm{surf}} - \sqrt{(x-x')^2+(y-y')^2}) \cdot \delta_{m,n}$$

$$S = \Delta x\Delta y \sum_{x,y} \exp\left(-\frac{(x-x')^2+(y-y')^2}{2\left[\sigma_{\mathrm{PBA}}(x', y'; z=0)\right]^2}\right),$$

$$m = \left\lfloor \frac{R}{\Delta R} + 0.5 \right\rfloor, n = \left\lfloor \frac{R_{\mathrm{res}}(x', y'; 0)}{\Delta R} + 0.5 \right\rfloor, \quad \text{(A6)}$$

where $R_{\mathrm{res}}(x, y; z)$ represents the residual range of the beams at a depth of z, which contributes to the point of interest (x,y). $H(a)$ is the step function, with $H(a \geq 0) = 1$ and $H(a < 0) = 0$, while Δx (or $\Delta x'$) and Δy (or $\Delta y'$) are the sizes of dose calculation grid in x and y, respectively. v_{surf}, the cutoff distance of pencil beam, is defined as $3\sigma_{\mathrm{PBA}}(x', y'; 0)$. $\delta_{m,n}$ is Kronecker delta. $\lfloor a \rfloor$ is the floor function, which gives the largest integer that is smaller than a. Since the pencil beam is much smaller than the beam interval close to the sampling plane, the usual normalization factor $2\pi\sigma^2$ has to be substituted by S. This normalization guarantees that the numerical integral dose in each slice is correct. When the spatial resampling procedure is additionally implemented at a depth of $z = d_{\mathrm{smp}}$, the fluence per residual range on the sampling plane d_{smp} is written as follows:

$$[\Phi(x, y; z = d_{\mathrm{smp}})]_R = \sum_{y'}\sum_{x'} \Delta x'\Delta y' \frac{[\Phi(x', y'; z = 0)]_R}{S} \times \exp\left(-\frac{(x-x')^2+(y-y')^2}{2\left[\sigma_{\mathrm{SR}_n}(x', y'; d_{\mathrm{smp}})\right]^2}\right) \times H(v_{\mathrm{smp}} - \sqrt{(x-x')^2+(y-y')^2}) \cdot \delta_{m,n}$$

$$S = \Delta x\Delta y \sum_{x,y} \exp\left(-\frac{(x-x')^2+(y-y')^2}{2[\sigma_{\mathrm{SR}_n}(x', y'; z = d_{\mathrm{smp}})]^2}\right),$$

$$m = \left\lfloor \frac{R}{\Delta R} + 0.5 \right\rfloor, n = \left\lfloor \frac{R_{\mathrm{res}}(x', y'; d_{\mathrm{smp}})}{\Delta R} + 0.5 \right\rfloor, \quad \text{(A7)}$$

where v_{smp}, the cutoff distance of sub-beam, is defined as $3\sigma_{\mathrm{SR}}(x', y'; d_{\mathrm{smp}})$. Consequently, from Eqs. (A6) and (A7), the dose at the point of interest (x, y, z) being deposited by sub-beams is given as follows:

$$D_{\mathrm{SR}}(x, y, z) = \sum_{R'=0}^{R_0}\sum_{y'}\sum_{x'} \Delta x'\Delta y' \left[\Phi(x', y'; z = 0 \text{ or } d_{\mathrm{smp}})\right]_{R'} \times \frac{C(x', y', WEL(x', y', z))}{S} \times \exp\left(-\frac{(x-x')^2+(y-y')^2}{2\left[\sigma_{\mathrm{SR}_n}(x', y'; z)\right]^2}\right)$$

$$S = \Delta x\Delta y \sum_{x,y} \exp\left(-\frac{(x-x')^2+(y-y')^2}{2\left[\sigma_{\mathrm{SR}_n}(x', y'; z)\right]^2}\right). \quad \text{(A8)}$$

APPENDIX C: APPLICATION OF THE SPATIAL RESAMPLING TECHNIQUE FOR A HEAD AND NECK TUMOR

To show the potential of the SRPBA to improve the accuracy of dosimetric calculations to the PBA, the spatial resampling technique was implemented for the pencil-beam calculation for a head and neck tumor with a volume of approximately 130 cm^3 from three gantry angles. We used the mono-energetic proton beam because it clarifies the improvement of the pencil-beam dose calculation. With the spatial resampling technique, an isocenter was chosen as a secondary resampling depth d_{smp}. The total dose distributions were normalized at the isocenter. The smearing distance of the range compensator[25] was taken at 4.5 mm. We monitored the minimum and maximum subtraction doses and the computing time. Figure 9 depicts the dose distributions in an axial plane obtained using (a) the PBA, (b) the PBA with resampling only at $z = 0$ minus the one without resampling, and (c) the PBA with resampling at $z = 0$ and $z = d_{\mathrm{smp}}$ minus the one without resampling In the figures, over/underestimations of dose regions were observed especially around the nasal sinus. The number of elemental pencil beams was 3581 in all algorithms on average. Minimum and maximum subtraction doses relative to the isocenter dose were (a) −15.1% and 9.70%, and (b) −17.9%

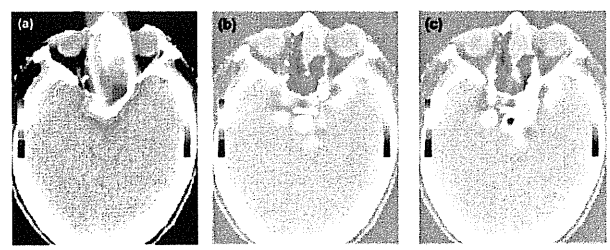

FIG. 9. Dose distributions in the axial plane of the patient with a head and neck tumor using (a) the PBA, (b) the PBA with resampling at $z = 0$ minus the PBA, and (c) the PBA with resampling at $z = 0$ and $z = d_{\mathrm{smp}}$ minus the PBA. Color bars are associated with dose values (×0.1% relative to the isocenter dose).

and 13.8%, respectively. The increases in computing time were factors of (a) 8.5 and (b) 20.

[a]Author to whom correspondence should be addressed. Electronic mail: egashira@nuclear.jp; Telephone: +81-3-5861-2958; Fax: +81-3-5861-2958.

[1]K. R Hogstrom, M. D. Michael, and P. R. Almond, "Electron beam dose calculations," Phys. Med. Biol. **26**, 446–460 (1981).
[2]P. L. Petti, "Differential-pencil-beam dose calculations for charged particles," Med. Phys. **19**, 137–149 (1992).
[3]L. Hong, M. Gotein, M. Buccuilini, R. Comiskey, B. Gottschalk, S. Rosenthal, C. Serago, and M. Urie, "Pencil beam algorithm for proton dose calculations," Phys. Med. Biol. **41**, 1305–1330 (1996).
[4]H. Szymanowski, A. Mazal, C. Nauaye, S. Biensan, R. Ferrand, M. C. Murillo, S. Caneva, G. Gaboriaud, and J. C. Rosenwald, "Experimental determination and verification of the parameters used in a proton pencil beam algorithm," Med. Phys. **28**, 975–987 (2001).
[5]B. Schaffner, E. Pedroni, and A. Lomax, "Dose calculation models for proton treatment planning using a dynamic beam delivery system: An attempt to include density heterogeneity effects in the analytical dose calculation," Phys. Med. Biol. **44**, 27–41 (1999).
[6]B. Schaffner, "Proton dose calculation based on in-air fluence measurements," Phys. Med. Biol. **53**, 1545–1562 (2008).
[7]N. Kanematsu, M. Komori, S. Yonai, and A. Ishizaki, "Dynamic splitting of Gaussian pencil beams in heterogeneity-correction algorithms for radiotherapy with heavy charged particles," Phys. Med. Biol. **54**, 2015–2027 (2009).
[8]N. Kanematsu, "Modeling of beam customization devices in the pencil-beam splitting algorithm for heavy charged particle radiotherapy," Phys. Med. Biol. **56**, 1361–1371 (2011).
[9]H. Szymanoqski and U. Oelfke, "Two-dimensional pencil beam scaling: An improved proton dose algorithm for heterogeneous media," Phys. Med. Biol. **47**, 3313–3330 (2002).
[10]L. Eyges, "Multiple scattering with energy loss," Phys. Rev. **74**, 1534–1535 (1948).
[11]A. S. Shiu and K. R. Hogstrom, "Pencil-beam redefinition algorithm for electron dose distributions," Med. Phys. **18**, 7–18 (1991).
[12]R. A. Boyd, K. R. Hogstrom, and G. Starkschall, "Electron pencil-beam redefinition algorithm dose calculations in the presence of heterogeneities" Med. Phys. **28**, 2096–2104 (2001).
[13]N. Kanematsu, S. Yonai, A. Ishizaki, and M. Torikoshi, "Computational modeling of beam-customization devices for heavy-charged-particle radiotherapy," Phys. Med. Biol. **53**, 3113–3127 (2008).
[14]V. L. Highland, "Some practical remarks on multiple scattering," Nucl. Instrum. Methods **129**, 497–499 (1975).
[15]V. L. Highland, "Some practical remarks on multiple scattering," Nucl. Instrum. Methods **161**, 171 (1979) (Erratum).
[16]T. Bortfeld and W. Schlegel, "An analytical approximation of depth-dose distribution for therapeutic proton beams," Phys. Med. Biol. **41**, 1331–1339 (1996).
[17]T. Nishio, "Present status and planning of facilities for proton and heavy ion cancer treatment in Japan—National Cancer Center," J. At. Energy Soc. **41** 1134–1138 (1999).
[18]T. Tachikawa, T. Sato, T. Ogino, and T. Nishio, "Proton beam therapy facilities of the National Cancer Center East Hospital," Radiat. Indust. **84**, 48–53 (1999).
[19]T. Nishio, S. Kataoka, M. Tachibana, K. Matsumura, N. Uzawa, H. Saito, T. Sasano, M. Yamaguchi, and T. Ogino, "Development of a simple control system for uniform proton dose distribution in a dual-ring double scattering method." Phys. Med. Biol. **51**, 1249–1260 (2006).
[20]E. Spezi, A. L. Angelini, F. Romani, and A. Ferri, "Characterization of a 2D ion chamber array for the verification of radiotherapy treatments," Phys. Med. Biol. **50**, 3361–3373 (2005).
[21]K. Hotta, R. Kohno, Y. Takada, Y. Hara, R. Tansho, T. Himukai, S. Kameoka, T. Matsuura, T. Nishio, and T. Ogino, "Improved dose-calculation accuracy in proton treatment planning using a simplified Monte Carlo method verified with three-dimensional measurements in an anthropomorphic phantom," Phys. Med. Biol. **55**, 3545–3556 (2010).
[22]R. Kohno, Y. Takada, T. Sakae, T. Terunuma, K. Matsumoto, A. Nohtomi, and H. Matsuda, "Experimental evaluation of validity of simplified Monte Carlo method in proton dose calculations," Phys. Med. Biol. **48**, 1277–1288 (2003).
[23]M. Goitein, "A technique for calculating the influence of thin inhomogeneities on charged particle beams," Med. Phys. **5**, 258–264 (1978).
[24]U. Schneider, B. Schaffner, T. Lomax, E. Pedroni, and A. Tourovsky, "A technique for calculating range spectra of charged particle beams distal to thick inhomogeneities," Med. Phys. **25**, 457–463 (1998).
[25]M. Urie, M. Goitein, and M. Wagner, "Compensating for heterogeneities in proton radiotherapy," Phys. Med. Biol. **29**, 533–566 (1984).

Journal of Radiation Research, 2012, 53, 588–593
doi: 10.1093/jrr/rrs010 Advance Access Publication 15 June 2012

Regular Paper

Impact of concurrent chemotherapy on definitive radiotherapy for women with FIGO IIIb cervical cancer

Yuuki KURODA[1,*], Naoya MURAKAMI[1], Madoka MOROTA[1], Shuhei SEKII[1], Kana TAKAHASHI[1], Koji INABA[1], Hiroshi MAYAHARA[1], Yoshinori ITO[1], Ryo-ichi YOSHIMURA[1], Minako SUMI[1], Yoshikazu KAGAMI[1], Noriyuki KATSUMATA[2], Takahiro KASAMATSU[3] and Jun ITAMI[1]

[1]Department of Radiation Oncology, National Cancer Center Hospital, Tokyo, Japan
[2]Department of Medical Oncology, National Cancer Center Hospital, Tokyo, Japan
[3]Department of Gynecologic Oncology, National Cancer Center Hospital, Tokyo, Japan
*Corresponding author. Department of Radiation Oncology, National Cancer Center Hospital, 5-1-1 Tsukiji Chuo-ku, Tokyo, Japan, 104-0045; Tel: 81-(3)3542-2511; Fax: 81-(3)3545-3567; Email: yuuki.kuroda.96@gmail.com

(Received 18 October 2011; revised 20 January 2012; accepted 7 February 2012)

The purpose of this retrospective study is to investigate the impact of concurrent chemotherapy on definitive radiotherapy for the International Federation of Gynecology and Obstetrics (FIGO) IIIb cervical cancer. Between 2000 and 2009, 131 women with FIGO IIIb cervical cancer were treated by definitive radiotherapy (i.e. whole pelvic external beam radiotherapy for 40–60 Gy in 20–30 fractions with or without center shielding and concomitant high-dose rate intracavitary brachytherapy with 192-iridium remote after loading system for 6 Gy to point A of the Manchester method). The concurrent chemotherapy regimen was cisplatin (40 mg/m^2/week). After a median follow-up period of 44.0 months (range 4.2–114.9 months) and 62.1 months for live patients, the five-year overall survival (OS), loco-regional control (LRC) and distant metastasis-free survival (DMFS) rates were 52.4, 80.1 and 59.9%, respectively. Univariate and multivariate analyses revealed that lack of concurrent chemotherapy was the most significant factor leading to poor prognosis for OS (HR = 2.53; 95% CI 1.44–4.47; $P = 0.001$) and DMFS (HR = 2.53; 95% CI 1.39–4.61; $P = 0.002$), but not for LRC (HR = 1.57; 95% CI 0.64–3.88; $P = 0.322$). The cumulative incidence rates of late rectal complications after definitive radiotherapy were not significantly different with or without concurrent chemotherapy (any grade at five years 23.9 vs 21.7%; $P = 0.669$). In conclusion, concurrent chemotherapy is valuable in definitive radiotherapy for Japanese women with FIGO IIIb cervical cancer.

Keywords: cervical cancer; IIIb; chemotherapy; radiotherapy; HDR

INTRODUCTION

External beam radiotherapy (EBRT) combined with intracavitary brachytherapy (ICBT) is the standard treatment for women with cervical cancer [1–3]. A combination of EBRT plus high-dose rate (HDR) ICBT for Japanese women with cervical cancer has provided acceptable outcomes and late complication rates despite the lower dose prescription in Japan than in the US [4–9]. In 2000s concurrent chemoradiotherapy (CCRT) became standard after the National Cancer Institute (NCI) announcement recommending concurrent chemotherapy in 1999 [10], however, the benefits of concurrent chemotherapy on definitive radiotherapy might not be applicable to concomitant EBRT plus HDR-ICBT and are not clear yet in Japan and other Asian countries [9]. We therefore performed a retrospective analysis in a mono-institutional group with newly diagnosed International Federation of Gynecology and Obstetrics (FIGO) IIIb cervical cancer treated by definitive radiotherapy, the purpose of this study being to investigate the impact of concurrent chemotherapy on definitive radiotherapy for Japanese women.

MATERIALS AND METHODS

Patients

We reviewed our database looking for women with newly diagnosed FIGO IIIb uterine cervical cancers with a

maximum diameter over 4 cm treated with definitive radiotherapy at the National Cancer Center Hospital between 2000 and 2009. Patients who received palliative EBRT alone, postoperative radiotherapy, interstitial brachytherapy or an experimental regimen of concurrent chemotherapy were excluded. A total of 131 women treated with EBRT plus HDR-ICBT were admitted to this retrospective analysis. All patients underwent pelvic examination, cystoscope, urography, computed tomography (CT), magnetic resonance imaging (MRI), ultrasound (US) and blood tests. Maximum tumor diameters were measured based on the MRI findings and/or US. FIGO staging was allocated for tumor boards of gynecological, medical and radiation oncologists. The pathological diagnosis was carried out with a central pathology review at our pathological division.

Treatment

Treatment selection was determined by the gynecological cancer board, our treatment policy for FIGO IIIb cervical cancer is CCRT to aim for loco-regional control (LRC) even if distant metastasis is not ruled out. Neoadjuvant chemotherapy was prohibited. The concurrent chemotherapy regimen was cisplatin (40 mg/m^2/week). Supportive treatments such as blood transfusions were encouraged during radiotherapy.

Radiotherapy

The radiotherapy field selected was the whole pelvis but exceptions were as follows: para-aortic node (PAN) area irradiation was acceptable in cases with suspicions of PAN metastasis, bilateral inguinal node area irradiation was acceptable in cases with vaginal involvement of more than two-thirds of total vaginal length. Radiotherapy doses of 40–60 Gy in 20–30 fractions were carried out with a 4-field box or the anterior–posterior technique. Center shield radiotherapy (CS) was performed for a shorter overall treatment time (OTT) reducing organ at risk (OAR) exposure depending on tumor shrinkage. CS was carried out 3–4 days/week, and HDR-ICBT 1–2 days/week, but both therapies were not carried out on the same day. All patients underwent EBRT with 10-, 15- and 20-MV X-rays from linear accelerators (Clinac IX, Varian, Palo Alto, CA, USA). Two-dimensional conventional radiotherapy (2DCRT) was employed between 2000 and 2005, and three-dimensional conformal radiotherapy (3DCRT) was used between 2005 and 2010. All patients underwent HDR-ICBT with 192-iridium remote after loading system (RALS, Microselectron). The point A dose prescription for 6 Gy using the Manchester method was performed with the ICBT planning system (Plato®, Nucletron). Image-guided optimization was not applicable even in the case of CT-based ICBT planning. A tandem-cylinder was used only in cases with vaginal involvement of more than one-third of total vaginal length or of an extraordinarily narrow vagina.

Follow-up

All patients were evaluated weekly for toxicity during radiotherapy through physical examinations and blood tests. CT and/or MRI scans and cytology were performed 1–3 months after radiotherapy for initial response, physical examination and blood tests were performed regularly every 1–6 months. Disease progression was defined by the response evaluation criteria in solid tumours (RECIST) version 1.1, new clinical symptoms or observable pelvic deficits.

Statistical analysis

Patient and treatment characteristics were compared using the Mann-Whitney *U* test and Pearson's chi-square test. OS was estimated from the beginning of radiotherapy to the date of death considered as an event, and censored at the time of last follow-up. LRC rate was estimated from the beginning of radiotherapy to the date of LRC failure including both central and lateral pelvic relapse considered as an event, and censored at the time of death or last follow-up. DMFS rate was estimated from the beginning of radiotherapy to the date of distant metastasis considered as an event, and censored at the time of death or last follow-up. The cumulative incidence rate of late rectal complication was estimated from the beginning of radiotherapy to the date of any grade rectal hemorrhage according to common terminology criteria for adverse events (CTCAE) version 4.0. [11] OS, LRC and DMFS, and the cumulative incidence rates of late rectal complication were calculated using the Kaplan–Meier method [12].

As a measure of radiotherapeutic intensity to point A, we used the equivalent dose in 2-Gy fractions (EQD_2) calculated from total irradiated dose (D) and each dose (d) with α/β for 10 Gy and potential doubling time (Tpot) defined as five days' subtraction from EQD_2 with correction for tumor proliferation associated with OTT (EQD_2T) as shown in the following formula:

$$EQD_2 = D\left(\frac{d+\alpha/\beta}{2+\alpha/\beta}\right)$$

$$\mathrm{EQD_2}T = \mathrm{EQD_2} - \frac{\log_{e^2}}{\alpha}\frac{\mathrm{T}-\mathrm{T}}{T_{pot}} \Big/ \left(1+\frac{2}{\alpha/\beta}\right)$$

T_K is the kick-off time of accelerated repopulation and was defined as 21 days, and 0.3 for α [13]. These parameters are not well estimated for cervical cancer so we used those for head and neck squamous cell carcinoma (SCC) and extrapolated them. The survival curves were compared using the log-rank test and Cox's proportional hazards model. In order to carry out univariate and/or multivariate

analysis comparing OS, LRC and DMFS rates, patients were categorized as follows: age (<60 vs ≥60), tumor bulk (<55 vs ≥55 mm), OTT (<6 vs ≥6 weeks), hemoglobin (Hb) before (<11.9 vs ≥11.9 mg/dl) and concurrent chemotherapy. We added univariate and multivariate analysis to assess the impact of concurrent chemotherapy on OS, LRC and DMFS after stratified analysis for age and tumor bulk. All statistical analyses were performed using PASW statistics (Version 18.0, SPSS Japan Inc., an IBM company, Chicago, IL, USA). A P value of <0.05 was considered significant.

RESULTS

Patient and treatment characteristics are shown in Table 1. There were differences in age and Hb level after treatment between the radiotherapy alone and CCRT groups. After a median follow-up period of 44.0 months (range 4.2–114.9 months) collectively and 62.1 months for live patients, five-year OS, LRC and DMFS rates were 52.4, 80.1 and 59.9%, respectively. Univariate and multivariate analyses revealed that default of concurrent chemotherapy was the most significant factor leading to poor prognosis for OS (HR = 2.53; 95% CI 1.44–4.47; $P = 0.001$) and DMFS (HR = 2.53; 95% CI 1.39–4.61; $P = 0.002$), but not for LRC (HR = 1.57; 95% CI 0.64–3.88; $P = 0.322$). (Table 2). The cumulative incidence rates of late rectal complications after definitive radiotherapy were not significantly different with or without concurrent chemotherapy (any grade at five years 23.9 vs 21.7%; $P = 0.669$) (Fig. 1). After stratifying 131 patients for age and tumor bulk, subgroup analysis with or without concurrent chemotherapy revealed that non-elderly women (HR = 2.78; 95% CI 1.25–6.18; $P = 0.012$) with even bulky length (HR = 2.53; 95% CI 1.26–5.07; $P = 0.009$) clearly benefit from concurrent chemotherapy (Table 3).

DISCUSSION

Various predictors such as treatment duration and anemia had been reported in the last decade before CCRT [14–18]. Concomitant EBRT with HDR-ICBT, which requires shorter treatment duration, was originally the mainstream treatment for women with cervical cancer in Japan [5]. Treatment durations of gross tumor irradiation had a median of 42 days, and were mostly 6 weeks, which is much shorter than the 8 weeks recommended by the American brachytherapy society (ABS) [14]. Concurrent chemotherapy has the potential hazard of treatment interruption associated with acute toxicities, however OTT was not significantly different between radiotherapy alone and CCRT (42 (30–69) vs 42 (36–62) days; $P = 0.217$). In this situation, OTT is no longer a prognostic factor [17]. Similarly, a low Hb value before radiotherapy has no impact on survival, and is no longer a prognostic factor if anemia has been actively corrected using blood transfusion during radiotherapy [18].

Randomized trials have shown survival benefits of CCRT for cervical cancer [19–23]. Incorporating concurrent chemotherapy contributed to improvement in both LRC and DMFS [19–23]. This impact is less in stages III–IV than in stages I–II [20–23]. Our study also supported this impact on OS and DMFS even in cases of FIGO IIIb, but not on LRC (Table 2). The cumulative incidence rates of late rectal complications after definitive radiotherapy were not significantly different with or without chemotherapy (any grade at five years 23.9 vs 21.7%; $P = 0.669$) and reached a plateau (Fig. 1), though limited by the short follow-up period for late radiation-induced complications of other organs such as bladder or small intestine [7].

There were important limitations on this retrospective analysis: the advantage of concurrent chemotherapy might merely indicate that the reasons for not undergoing concurrent chemotherapy were associated with poor prognosis. Forty-two women with FIGO IIIb cervical cancer did not undergo concurrent chemotherapy in our study because of advanced age (77 (72–85) years) for 17 patients (40.4%), and the other half (53 (36–70)) had the following reasons for not undergoing concurrent chemotherapy:PAN irradiation for eight patients (19.0%), renal failure for three patients (7.2%), lack of patient's consent for five patients (11.9%), chronic hepatitis for two patients (4.8%), active pyometra, uncontrolled anemia, synchronous double cancer, hypertrophic cardiomyopathy, low white blood cell counts and sequential chemotherapy for one patient each (2.4%). These reasons not to perform concurrent chemotherapy seem to be clinically ordinary and acceptable, but could indicate a potential selection bias that modified the impact of concurrent chemotherapy. Our study revealed that concurrent chemotherapy is the most significant predictor of definitive radiotherapy, thus we conclude that concurrent chemotherapy combined with definitive radiotherapy for FIGO IIIb cervical cancer is advantageous for survival improvement.

Development of the optimal chemotherapy regimen and schedule to increase chemotherapeutic intensity as a cytotoxic agent but not a radiosensitizer seems to be warranted because our results indicated concurrent chemotherapy has impacts on DMFS but not on LRC. It is not reasonable for Japanese women with cervical cancer to undergo increased intensity of dose-dense concurrent chemotherapy due to a lack of relevant feasibility [24]. There is no evidence that platinum-doublet is superior to platinum-alone as concurrent chemotherapy for cervical cancer [22–23]. Therefore, devising the best form of concurrent chemotherapy is considered to be a limitation. The efficacy of adjuvant chemotherapy after definitive CCRT is unclear but worth testing as it is a feasible method [25].

Table 1. Patient and treatment characteristics for RT alone and CCRT

		RT alone ($n = 42$)	CCRT ($n = 89$)	P
Age	Median (range)	66 (36–85)	55 (29–73)	0.000
Tumor bulk	mm	55 (45–87)	55 (40–95)	0.302
Pathology	SCC	37 (88.1%)	82 (92.1%)	0.454
	non-SCC	5 (11.9%)	7 (7.9%)	
Hb before RT	mg/dl	11.9 (6.4–14.2)	11.9 (7.1–14.5)	0.653
Hb after RT	mg/dl	11.3 (7.6–14.4)	10.3 (6.9–12.3)	0.002
OTT	days	42 (30–69)	42 (36–62)	0.217
EQD_2	Gy	56.4 (44.0–74.0)	54.0 (52.2–74.0)	0.128
EQD_2T	Gy	50.0 (40.9–66.2)	48.2 (39.2–61.2)	0.177
wCDDP courses	1	0	5 (5.6%)	0.000
	2	0	6 (6.8%)	
	3	0	12 (13.5%)	
	4	0	23 (25.8%)	
	5	0	30 (33.7%)	
	6	0	13 (14.6%)	
Reason for RT alone	Advanced age	17 (40.4%)	0	0.000
	PAN irradiation	8 (19.0%)	0	
	No consent	5 (11.9%)	0	
	Renal function	3 (7.2%)	0	
	Hepatitis	2 (4.8%)	0	
	Others	7 (16.7%)	0	
Follow-up	months	30.7 (4.2–100.3)	48.8 (7.3–114.9)	0.001

RT = radiotherapy, CCRT = concurrent chemoradiotherapy, FIGO = International Federation of Gynecology and Obstetrics, SCC = squamous cell carcinoma, Hb = hemoglobin, OTT = overall treatment time, EQD_2 = the equivalent dose in 2-Gy fractions, $EQD_2T = EQD_2$ with correction for tumor proliferation associated with OTT, wCDDP = weekly cisplatin, ns = not significant.

Table 2. Univariate and multivariate analyses on OS, LRC and DMFS

			OS			LRC			DMFS		
Variants		n	**Five years**	**uni**	**multi**	**Five years**	**uni**	**multi**	**Five years**	**uni**	**multi**
Age	<60	72	51.4	0.631	0.121	73.3	0.129	0.076	56.0	0.173	0.033
	≥60	59	53.7			89.2			64.8		
Tumor bulk	<55 mm	54	59.8	0.358	0.486	79.5	0.768	0.856	74.4	0.010	0.027
	≥55 mm	77	47.6			80.6			50.2		
OTT	<6 weeks	75	53.1	0.789	0.639	78.5	0.532	0.258	63.5	0.626	0.918
	≥6 weeks	56	50.8			82.6			56.0		
Hb before RT	<11.9 mg/dl	62	53.1	0.627	0.934	74.5	0.380	0.599	59.3	0.527	0.988
	≥11.9 mg/dl	69	52.2			84.8			60.6		
Concurrent chemotherapy	Yes	89	60.4	0.002	0.001	82.6	0.583	0.322	66.6	0.005	0.002
	No	42	33.5			68.3			44.7		

OS = overall survival, LRC = loco-regional control, DFMS = distant metastasis free survival, uni = univariate analysis, multi = multivariate analysis, OTT = overall treatment time, Hb = hemoglobin, ns = not significant.

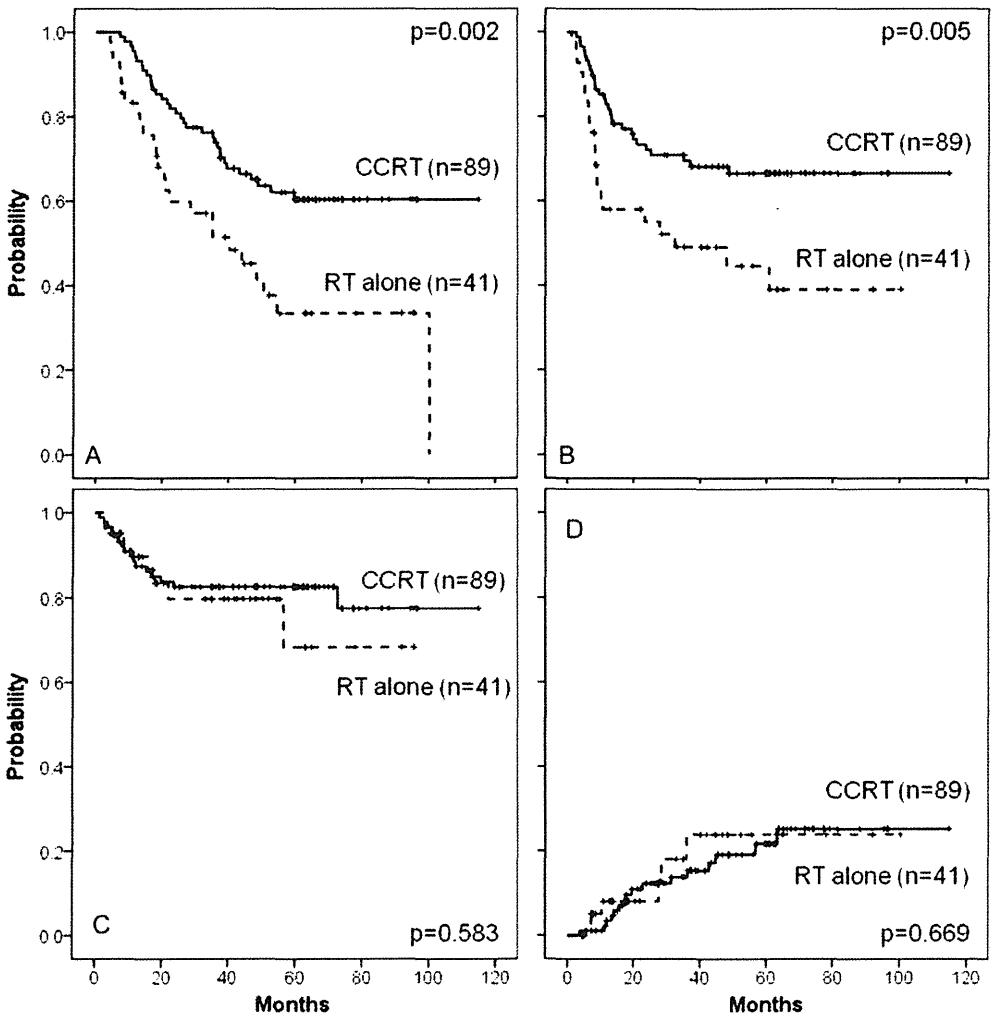

Fig. 1. OS (**A**), DMFS (**B**), LRC (**C**) and the cumulative incidence rates of late rectal complication (**D**) of women with FIGO IIIb cervical cancer after definitive radiotherapy with or without concurrent chemotherapy. Solid line for CCRT, dashed line for RT alone. OS = overall survival, DMFS = distant metastasis free survival, LRC = loco-regional control, CCRT = concurrent chemoradiotherapy, RT = radiotherapy.

Table 3. Impact of concurrent chemotherapy on OS, LRC and DMFS in the stratified analysis

		OS			LRC			DMFS		
		Log-rank	Cox's		Log-rank	Cox's		Log-rank	Cox's	
Variates		*P*	HR (95%CI)	*P*	*P*	HR (95%CI)	*P*	*P*	HR (95%CI)	*P*
Age	<60	0.005	2.78 (1.25–6.18)	0.012	0.145	2.31 (0.76–6.96)	0.136	0.001	2.83 (1.32–6.05)	0.007
	≥60	0.023	2.55 (1.10–5.89)	0.028	0.942	1.05 (0.23–4.85)	0.942	0.079	2.29 (0.88–5.94)	0.087
Tumor bulk	<55 mm	0.118	2.36 (0.85–6.52)	0.096	0.108	5.87 (1.27–27.0)	0.023	0.043	3.46 (1.01–11.9)	0.049
	≥55 mm	0.018	2.53 (1.26–5.07)	0.009	0.587	0.75 (0.22–2.49)	0.645	0.085	2.23 (1.12–4.44)	0.021

OS = overall survival, DMFS = distant metastasis free survival, ns = not significant.

In conclusion, though limited to a mono-institutional retrospective analysis, this study revealed that concurrent chemotherapy is valuable in definitive radiotherapy for Japanese women with FIGO IIIb cervical cancer. A randomized controlled trial is needed to establish the optimal chemotherapy combined with definitive radiotherapy for women with advanced cervical cancer.

ACKNOWLEDGEMENTS

We declare no conflict of interest. This work was partly supported by a Grant-in-Aid from the Tohoku Cancer EBM project of Yamagata University Faculity of Medicine, Cancer Research Development Fund, National Cancer Center.

REFERENCES

1. Thoms WW, Jr, Eifel PJ, Smith TL *et al.* Bulky endocervical carcinoma: a 23-year experience. *Int J Radiat Oncol Biol Phys* 1992;**23**:491–9.
2. Perez CA, Grigsby PW, Nene SM *et al.* Effect of tumor size on the prognosis of carcinoma of the uterine cervix treated with irradiation alone. *Cancer* 1992;**69**:2796–806.
3. Landoni F, Maneo A, Colombo A *et al.* Randomised study of radical surgery versus radiotherapy for stage Ib-IIa cervical cancer *Lancet* 1997;**350**:535–40.
4. Eifel PJ, Moughan J, Erickson B *et al.* Patterns of radiotherapy practice for patients with carcinoma of the uterine cervix: a patterns of care study. *Int J Radiat Oncol Biol Phys* 2004;**60**:1144–53.
5. Toita T, Kodaira T, Shinoda A *et al.* Patterns of radiotherapy practice for patients with cervical cancer (1999–2001): patterns of care study in Japan. *Int J Radiat Oncol Biol Phys 2008*;**70**:788–94.
6. Toita T, Kato S, Niibe Y *et al.* Prospective multi-institutional study of definitive radiotherapy with high-dose-rate intracavitary brachytherapy in patients with nonbulky (<4-cm) stage i and ii uterine cervical cancer (JAROG0401/JROSG04-2). *Int J Radiat Oncol Biol Phys* 2012;**82**:49–56.
7. Nakano T, Kato S, Ohno T *et al.* Long-term results of high-dose rate intracavitary brachytherapy for squamous cell carcinoma of the uterine cervix. *Cancer* 2005;**103**:92–101.
8. Toita T, Moromizato H, Ogawa K *et al.* Concurrent chemoradiotherapy using high-dose-rate intracavitary brachytherapy for uterine cervical cancer. *Gynecol Oncol* 2005;**96**:665–70.
9. Nagase S, Inoue Y, Umesaki N *et al.* Evidence-based guidelines for treatment of cervical cancer in Japan: Japan Society of Gynecologic Oncology (JSGO) 2007 edition. *Int J Clin Oncol* 2010;**15**:117–24.
10. NCI Issues Clinical Announcement on Cervical Cancer: Chemotherapy Plus Radiation Improves Survival. http://www.nih.gov/news/pr/feb99/nci-22.htm (11 April 2012, date last accessed).
11. National Cancer Institute Common Terminology Criteria for Adverse Events (CTCAE) version 4.03, 2010. http://evs.nci.nih.gov/ftp1/CTCAE/CTCAE_4.03_2010-06-14_QuickReference_5x7.pdf (10 April 2012, date last accessed).
12. Kaplan EL, Meier P Nonparametric estimation from incomplete observations *J Am StatAssoc* 1958;**53**:457–81.
13. Hall EJ, Giaccia AJ. *Radiobiology for the Radiologist: Time, Dose, and Fractionation in Radiotherapy, 6th edn.* Philadelphia: Lippincott Williams & Wilkins, 2006, 378–97.
14. Nag S, Erickson B, Thomadsen B *et al.* The American Brachytherapy Society recommendations for high-dose-rate brachytherapy for carcinoma of the cervix. *Int J Radiat Oncol Biol Phys* 2000;**48**:201–11.
15. Lanciano RM, Martz K, Coia LR *et al.* Tumor and treatment factors improving outcome in stage III-B cervix cancer. *Int J Radiat Oncol Biol Phys* 1991;**20**:95–100.
16. Toita T, Kakinohana Y, Ogawa K *et al.* Combination external beam radiotherapy and high-dose-rate intracavitary brachytherapy for uterine cervical cancer: analysis of dose and fractionation schedule. *Int J Radiat Oncol Biol Phys* 2003;**56**:1344–53.
17. Chatani M, Matayoshi Y, Masaki N *et al.* High-dose rate intracavitary irradiation for carcinoma of the uterine cervix. The adverse effect of treatment prolongation. *Strahlenther Onkol* 1997;**173**:379–84.
18. Grogan M, Thomas GM, Melamed I *et al.* The importance of hemoglobin levels during radiotherapy for carcinoma of the cervix. *Cancer* 1999;**86**:1528–36.
19. Rose PG, Bundy BN, Watkins EB *et al.* Concurrent cisplatin-based radiotherapy and chemotherapy for locally advanced cervical cancer. *N Engl J Med* 1999;**340**:1144–53.
20. Morris M, Eifel PJ, Lu J *et al.* Pelvic radiation with concurrent chemotherapy compared with pelvic and para-aortic radiation for high-risk cervical cancer. *N Engl J Med* 1999;**340**:1137–43.
21. Eifel PJ, Winter K, Morris M *et al.* Pelvic irradiation with concurrent chemotherapy versus pelvic and para-aortic irradiation for high-risk cervical cancer: an update of radiation therapy oncology group trial (RTOG) 90-01. *J Clin Oncol* 2004;**22**:872–80.
22. Green JA, Kirwan JM, Tierney JF *et al.* Survival and recurrence after concomitant chemotherapy and radiotherapy for cancer of the uterine cervix: a systematic review and meta-analysis. *Lancet* 2001;**358**:781–6.
23. Chemoradiotherapy for Cervical Cancer Meta-Analysis Collaboration. Reducing uncertainties about the effects of chemoradiotherapy for cervical cancer: a systematic review and meta-analysis of individual patient data from 18 randomized trials. *J Clin Oncol* 2008;**26**:5802–12.
24. Watanabe Y, Nakai H, Shimaoka M *et al.* Feasibility of concurrent cisplatin use during primary and adjuvant chemoradiation therapy: a phase I study in Japanese patients with cancer of the uterine cervix. *Int J Clin Oncol* 2006;**11**:309–13.
25. Dueñas-González A, Zarbá JJ, Patel F *et al.* Phase III, open-label, randomized study comparing concurrent gemcitabine plus cisplatin and radiation followed by adjuvant gemcitabine and cisplatin versus concurrent cisplatin and radiation in patients with stage IIB to IVA carcinoma of the cervix. *J Clin Oncol* 2011;**29**:1678–85.

International Journal of
Radiation Oncology
biology • physics

www.redjournal.org

Clinical Investigation: Central Nervous System Tumor

^{106}Ruthenium Plaque Therapy (RPT) for Retinoblastoma

Naoya Murakami, MD,* Shigenobu Suzuki, MD,† Yoshinori Ito, MD,* Ryoichi Yoshimura, MD, PhD,‡ Koji Inaba, MD,* Yuki Kuroda, MD,* Madoka Morota, MD, PhD,* Hiroshi Mayahara, MD, PhD,* Mototake Sakudo, MS,* Akihisa Wakita, MS,* Hiroyuki Okamoto, MS,* Minako Sumi, MD, PhD,* Yoshikazu Kagami, MD,* Keiichi Nakagawa, MD, PhD,§ Kuni Ohtomo, MD, PhD,§ and Jun Itami, MD, PhD*

*Departments of *Radiation Oncology and †Ophthalmic Oncology, National Cancer Center Hospital, Tokyo, Japan; ‡Department of Diagnostic Radiology and Oncology, Head and Neck Reconstruction Division, Graduate School, Tokyo Medical and Dental University, Tokyo, Japan; and §Department of Radiology, University of Tokyo Hospital, Tokyo, Japan*

Received Mar 13, 2011, and in revised form Oct 30, 2011. Accepted for publication Nov 1, 2011

Summary

One hundred one ^{106}ruthenium plaque therapies were retrospectively analyzed that were performed in 90 eyes of 85 patients with retinoblastoma between 1998 and 2008.

Purpose: To evaluate the effectiveness of episcleral ^{106}ruthenium plaque therapy (RPT) in the management of retinoblastoma.

Methods and Materials: One hundred one RPTs were retrospectively analyzed that were performed in 90 eyes of 85 patients with retinoblastoma at National Cancer Center Hospital between 1998 and 2008. Each RPT had a corresponding tumor and 101 tumors were considered in the analysis of local control. Median follow-up length was 72.8 months. Median patient age at the RPT was 28 months. Median prescribed doses at reference depth and outer surface of the sclera were 47.4 Gy and 162.3 Gy, respectively.

Results: Local control rate (LCR) and ocular retention rate (ORR) at 2 years were 33.7% and 58.7%, respectively. Unilateral disease, International Classification of Retinoblastoma group C or more advanced at the first presentation or at the time of RPT, vitreous and/or subretinal seeding, tumor size greater than 5 disc diameter (DD), reference depth greater than 5 mm, dose rate at reference depth lower than 0.7 Gy/hour, dose at the reference depth lower than 35 Gy, and (biologically effective dose with an α/β ratio of 10 Gy) at the reference depth lower than 40 Gy_{10} were associated with unfavorable LCR. Two patients died of metastatic disease. Radiation complications included retinal detachment in 12 eyes (13.3%), proliferative retinopathy in 6 (6.7%), rubeosis iris in 2 (2.2%), and posterior subcapsular cataract in 23 (25.6%).

Conclusion: RPT is an effective eye-preserving treatment for retinoblastoma.

Introduction

Retinoblastoma is the most common intraocular malignancy of childhood that arises from neuroepithelial cells of the retina. The reported incidence of retinoblastoma is 1 in 16,653-22,166 live births in Japan (1).

For the management of children with retinoblastoma, mutilating enucleation and external beam radiation therapy (EBRT) are

Reprint requests to: Naoya Murakami, MD, Department of Radiation Oncology, National Cancer Center Hospital, 5-1-1, Tsukiji Chuo-ku, Tokyo 104-0045, Japan. Tel: +[81]-3-3542-2511; Fax: +[81]-3-3545-3567; E-mail: namuraka@ncc.go.jp

Conflict of interest: none.

Int J Radiation Oncol Biol Phys, Vol. 84, No. 1, pp. 59–65, 2012
0360-3016/$ - see front matter
doi:10.1016/j.ijrobp.2011.11.002

employed with a decreasing frequency, because of the facial disfigurement and increased incidence of the secondary malignancies after EBRT (2). Chemotherapy has been replacing EBRT as the modality for organ preservation (3, 4). Although chemotherapy can shrink the retinoblastoma lesion, local therapy is indispensable to attain local control. Episcleral plaque brachytherapy has emerged as a treatment option as a focal therapy in the primary or secondary treatment of retinoblastoma (3-5). Low-energy gamma-ray emitting ^{125}I plaque is most used around the world, which is inexpensive and can be customized to fit each tumor shape by arranging seed locations in the episcleral applicator (5-7). In contrast, the pure beta ray-emitting ^{106}ruthenium (^{106}Ru) plaque is used mainly in Europe (8, 9). Although ^{106}Ru plaque is very expensive and cannot treat tumors with a height greater than 5-6 mm because it emits purely beta rays (energy 3.54 MeV) (8-11), the thickness of the applicators is only 1 mm in contrast to 3 mm thickness of the I-125 applicators, which is greatly advantageous when an infant's very small eyes are dealt with. In Japan, National Cancer Center Hospital is the only institution performing episcleral brachytherapy using ^{106}Ru plaque applicators. This retrospective study analyzes the results of ^{106}Ru plaque therapy (RPT) in the management of retinoblastoma.

Methods and Materials

We retrospectively reviewed the clinical records of all patients undergoing RPTs for retinoblastoma between December 1998 and November 2008 in the National Cancer Center Hospital, Japan. One hundred one tumors of 90 eyes in 85 patients were treated by RPT during this period. In 10 eyes, multiple tumors were treated by simultaneous application of the plaques. Local status of the 101 tumors could be evaluated. All tumors were followed at least for 1 year. Patient and tumor characteristics at the initial presentation are listed in Table 1. Tumor stage is based on International Classification of Retinoblastoma (ICRB) (4, 12, 13). Only 31 (30.7%) of the 101 tumors presented with confined diseases of group A or B. Vitreous and subretinal tumor seedings were seen in 41.6% and 35.6%, respectively.

When RPT was the initial treatment, it was considered as the first-line treatment. When RPT followed after local and/or systemic therapies that had successfully reduced the tumor, it was considered as the second-line treatment. RPT was considered as salvage therapy, provided that it was employed to treat a refractory or relapsed tumor after the preceding therapies. In the current series, RPT was employed in only 4 tumors as the first-line therapy. The other 62 tumors underwent RPT as the second-line therapy and 35 as salvage therapy (Table 2). Some too-large tumors, apparently not suitable to be treated by RPT, underwent RPTs, because there was a strong wish of the parents to conserve

Table 1 Characteristics of patients and 101 tumors at the initial presentation

Characteristics	Number
Patients	85
Gender	
Male	52
Female	33
Age at the first brachytherapy	28 mo (range 7-240)
Laterality	
Bilateral	60
Unilateral	25
Family history	
Positive	9
ICRB	
Group A	2 (2.0%)
Group B	29 (28.7%)
Group C	15 (14.9%)
Group D	43 (42.6%)
Group E	7 (6.9%)
Unknown	5 (5.0%)
Tumor with vitreous seeding	42 (41.6%)
Tumor with subretinal seeding	36 (35.6%)
Median tumor size	5 DD (range 0.8-20)

Abbreviations: DD = disc diameter; ICRB = International Classification of Retinoblastoma.

Table 2 Tumor and treatment characteristics at the 101 first RPTs

Tumor characteristics	Number (%)
First-line therapy	4 (4.0)
Second-line therapy	62 (61.4)
Salvage therapy	35 (34.6)
ICRB at brachytherapy	
Group A	9 (8.9)
Group B	29 (28.7)
Group C	20 (19.8)
Group D	37 (36.6)
Group E	6 (5.9)
Tumor with subretinal seeding	28 (27.7)
Tumor with vitreous seeding	42 (41.6)
Response to preceding therapy	
Good	34 (33.7)
Stable	41 (40.6)
Poor	17 (16.8)
Unknown	5 (5.0)
Tumor size (DD)	
Median	5 DD (range 0.5-22)
Brachytherapy dose at outer surface of sclera	
Median	162.3 Gy (range: 61.3-950.0)
Brachytherapy dose at outer surface of sclera (BED_3)	
Median	854.9 Gy_3 (range 101.2-4317.0)
Dose rate at outer surface of sclera	
Median	7.5 Gy/h (range 4.5-10.3)
Brachytherapy reference depth	
Median	5 mm (range 3-9)
Dose rate at reference depth	
Median	0.83 Gy/h (range 0.11-2.22)
Brachytherapy dose at reference depth	
Median	47.4 Gy (range 24.3-86.1)
Brachytherapy dose at reference depth (BED_{10})	
Median	65.6 Gy_{10} (range 27.0-131.3)
Brachytherapy treatment time	
Median	53.3 h (range: 20.5-332.3)

Abbreviations: BED = biological effective dose; DD = disc diameter; ICRB = the International Classification of Retinoblastoma; RPT = ruthenium plaque brachytherapy.